Validation of a modelling methodology for wind turbine rotor blades based on a full scale blade test

Pablo Noever-Castelos[1], Bernd Haller[2], and Claudio Balzani[1]

[1]Leibniz University Hannover, Institute for Wind Energy Systems, Appelstr. 9A, Hanover, 30167, Germany
[2]Fraunhofer Institute for Wind Energy Systems IWES, Am Seedeich 45, 27572 Bremerhaven, Germany

Correspondence: Pablo Noever-Castelos (research@iwes.uni-hannover.de)

Abstract. Detailed 3D finite element simulations are state of the art for structural analyses of wind turbine rotor blades. It is of utmost importance to validate the underlying modelling methodology in order to obtain reliable results. Validation of the global response can ideally be done by comparing simulations with full scale blade tests. However, there is a lack of test results for which the blade data are completely available.

5   The aim of this paper is to validate one particular blade modelling methodology that is implemented in an in-house model generator, and to provide respective test results to the public. A hybrid 3D shell/solid element model is created including the respective boundary conditions. The problem is solved via a commercially available finite element code. A full scale blade test is performed as the validation reference, for which all relevant data are available. Some data have been measured prior to or after the test in order to account for manufacturing deviations. The tests comprise classical bending tests in flap-wise and lead-lag direction as well as torsion tests.

10   For the validation of the modelling methodology, global blade characteristics from measurements and simulation are compared. These include the overall mass and centre of gravity as well as their distributions along the blade, deflections, strain levels, and natural frequencies and modes. Overall, good agreement is obtained, though some improvements might be required for the response in torsion. As a conclusion, the modelling strategy can be rated as validated.

1 Introduction

Rotor blades are major components of wind turbines. They are susceptible to damages, which, in case they need repair, can result in severe turbine downtimes (Reder et al., 2016). It is thus crucial to develop a blade design that withstands all designated loads without damage. Though a blade prototype is always tested at the full blade scale in the certification process (International Eletrotechnical Comission, 2014), such tests are very costly and time-consuming, especially for growing blade dimensions (Ha et al., 2020). For this reason, full scale blade tests are executed one time only for the final validation of design assumptions. Hence, a reliable and fast virtual blade design procedure is required. Full 3D finite element (FE) analysis is accurate but computationally expensive. A widely used approach for wind turbine blade design is to carry out two-dimensional cross-sectional analyses that offer a reduced level of complexity but are a fast and efficient alternative for rotor blade pre-designs (Chen et al., 2010). Tools like VABS (Yu et al., 2002) or BECAS (DTU Wind Energy) compute cross-sectional properties based

25 on a 2D-FE-analysis, which are necessary to feed the aero-elastic models in order to recalculate the design loads on the turbine

blades and close the design iteration loop. Nevertheless, at a final stage 3D FE analyses have to be performed in order to obtain

a reliable blade design and double check structural details such as adhesive joints, geometric discontinuities, ply drops, etc.

Automated model creation is state of the art and a key to enhance the design process significantly by reducing time con-

sumption, increasing the possible number of design loops and avoiding modelling errors. Among a vast selection of common

30 software tools originated from the scientific community, QBlade (D. Marten et al., 2013) for example focuses on the aero-

dynamic blade design, neglecting details on structural information. Sandia's NuMAD (Jonathan C. Berg and Brian R. Resor,

2012) additionally contains a more sophisticated structural description taking into account a proper composite definition for the

blades' subcomponents. Same holds for the software package FOCUS developed by WMC Laboratories which is now part of

LM Wind Power (N. P. Duineveld, 2008), which is a state of the art tool used for blade design in many engineering offices. In

35 FOCUS the user discretizes a few stations in span-wise direction with all necessary geometrical information of these particular

cross-section and in between the tool interpolates linearly all missing data. Hence a high discretization of stations along the

blade span is necessary to correctly reproduce non-linear changing geometrical or material information in span-wise direction.

Another more advanced tool is the optimization framework CP-Max, see Bottasso et al. (2014). The parametrization is based

on mathematical functions for the blade design description in span-wise direction. This method has the advantage of reducing

40 the number of stations along the blade without loosing information in between, while enabling the framework to efficiently

manipulate the parameters during optimization. The focus of the optimization framework is to find a solution at minimum

costs. A similar blade parametrization is used within the FUSED-Wind Framework (Zahle et al., 2020), which contains spline

descriptions for each parameter as shown in the prominent example of the DTU 10MW reference blade design (C. Bak et al.,

2013). An interface to the framework was later incorporated into the python-tool FEPROC and the correct modelling process

45 was verified against the DTU 10MW reference blade (Rosemeier, 2018). Another blade modelling tool developed at Ghent

University also relies on function-based descriptions of the blade parameters and focuses on a modular principle of Finite

Element (FE) constellations for modelling the different blade components and joints in the structure (Peeters et al., 2018). The

latter algorithm and CP-Max are able of generating solid element models, while the others rely on more common shell element

representations.

50 Though some of these model creation frameworks may work with functions or splines describing the blade's geometrical or

layup information, most of them work with a reasonably high number of airfoils/stations that in addition to the blade's geometry

yield the outer blade shape by a global linear or higher order interpolation between the airfoils. Similar to Rosemeier (2018),

who uses Parametric Geometry Library (PGL, Zahle (2020)) to interpolate additional airfoils, the presented algorithm in this

work generates airfoils independent from the other parameters and uses the relative thickness distribution to position these

55 along the span. Additionally a more detailed adaption of blade and material parameters is implemented to consider changes

along the span for all characteristics of the blade's structure.

A lot of scientific contributions deal with FE modelling and focus on structural details like trailing edge adhesive joints. Eder

and Bitsche (2015) for instance use a local model with fracture analysis to deduce the debonding between shell and adhesive

due to buckling and validate the behaviour against experimental results. Ji and Han (2014) also apply fracture mechanics and

60   use a detailed model at the shear web adhesive joint to analyse crack propagation in the bond line. Most of these locally detailed models are used within a global-local modelling approach like in Chen et al. (2014) to reduce the global model complexity while keeping a high level of detail at local spots. However, this paper focuses on the global elastic response of wind turbine blades, so there is no need for local sub-models.

Different FE modelling procedures can result in different deformation and stress solutions, though based on the same model

65   parameters, see (Lekou et al., 2015). Hence, it is important to validate modelling strategies by comparing simulations with full blade tests, which is the aim of this paper. A quasi-static full scale blade test is performed, including not only bending tests in flap and lead-lag direction – as are usually executed in the context of blade certification (International Eletrotechnical Comission, 2014) – but also torsion tests. This allows for an exceptionally detailed and thorough validation. Unlike other blade tests reported in literature (**?**), (Chen et al., 2017), (Jensen et al., 2006), (Overgaard and Lund, 2010), (Overgaard et al., 2010), the

70   aim of the tests in this work is not the validation of failure models. Hence, the blade is not loaded up to failure. The aim rather is to measure the global blade behaviour expressed in terms of deflections, strains, mass distribution, and modal characteristics and to validate our own blade modelling technique. The blade under investigation is the SmartBlades DemoBlade (REFERENCE TO COME), a 20 m blade including pre-bend and pre-sweep towards the trailing edge. The blade is modelled with our in-house blade model creation tool MoCA (Model Creation and Analysis Tool for Wind Turbine Rotor Blades), taking into

75   account some major manufacturing-related deviations. The test setup and the load introduction are approximated via a combination of suitable boundary conditions and multiple point constraints. The simulation results are thoroughly compared with the test measurements. Generally good agreement is observed, especially for the bending loads. However, some improvements may be required for accurately modelling the torsional behaviour of the blade.

The modelling strategy is addressed in section 2 and section 3. The test setup is described in section 4. The blade was cut into

80   segments after the tests in order to accurately measure the mass distribution and the locations of the centres of gravity along the blade. These measurements are also described in section 4. The simulation versus test comparison is reported in section 5, followed by the conclusions in section 6.

2   Model Creation Framework

A framework to automatically generate fully parameterized 3D FE models of wind turbine rotor blades from a set of parameters

85   was developed at the Institute for Wind Energy Systems at Leibniz University Hannover. The purpose of this tool called MoCA (**Mo**del **C**reation and **A**nalysis Tool for Wind Turbine Rotor Blades) is to enable users to investigate and analyse different blade designs or design parameter variations in an efficient way, including structural details such as e. g. adhesive joints. The following section presents a brief description of the framework.

MoCA is based on a set of input parameters categorised in *Geometry*, *Plybook*, *Structure*, and *Material*. In general all

90   parameters that describe a distribution along the blade are stored as splines over the blade's arc length, but even material parameters may be varied over the blade arc if necessary by using a spline. The parameter set *Geometry* contains all information on the outer geometry of the blade, i. e. the airfoils used and their positions along the blade as well as the distributions of the

relative thickness, chord length, twist angle, threading point location, prebend and presweep. The *Structure* set is associated

with the structural description of the blade. This includes the specification of shear webs, adhesive joints and additional masses

95   as well as cross-sectional division points that are mainly used to subdivide cross-sections into different regions of interest.

The *Plybook* parameters contain the stacking information of different composite layups used in the blade. The parameter set

Material comprises all material properties assigned for the different materials. These can either be isotropic or anisotropic on

the macroscopic scale. The user can also specify a composite material based on microscopic characteristics of the fibre and

matrix constituents, which are then transformed to a laminate via the well-known rule of mixtures.

100   The flowchart in figure 1 depicts the structure of the finite element creation procedure implemented in MoCA on the basis

of the parameter sets described above. First, the blade segmentation, i. e. the discretization in span-wise direction, is defined.

For each blade segment edge, a cross-section of the blade is calculated by evaluating the *Geometry* data. Then a finite element

discretization of the cross-sections is executed using the information of the *Structure*, *Material*, and *Plybook* parameter blocks.

At this stage, an interface to the BECAS (DTU Wind Energy) software can be utilized to calculate the full 6×6 stiffness

105   and mass matrices of a beam model. However, since our aim is to create a 3D blade model, we continue with the finite

element discretization in span-wise direction utilising a hybrid shell element/solid element strategy. Therein, we use shell

elements to model the composite laminates and solid elements for the adhesives. The 3D FE mesh includes the node-to-

element connectivity and elemental material assignments. The boundary conditions are added and the FE model is translated to

an input file for the finite element solver of choice, which in our case is ANSYS Mechanical (ANSYS Inc.). In the following,

110   we describe in more detail the different steps of this overall procedure.
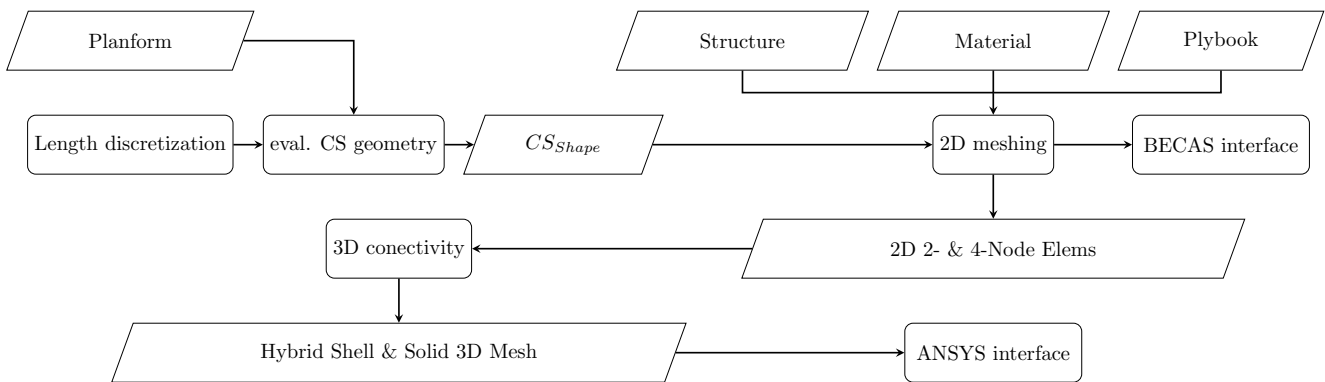

Figure 1. Flowchart of the finite element model creation procedure in MoCA.

Figure 2 visualises the process of cross-section geometry calculation. After the blade segmentation, the *Geometry* data

splines are evaluated for the particular blade arc positions of the segment edges. Based on the spline-based interpolation of the

relative thickness t_{rel}, an airfoil AF is linearly interpolated between the basic input airfoils with the next higher and lower

relative thickness. In contrast to a global blade shape interpolation, the use of a blade independent airfoil interpolation enables

115   the user to implement an own sub-function and replacing the former. The interpolated airfoils are then scaled by the chord

length c^* calculated via the respective spline, shifted along the chord to the correct threading point by the coordinate tp^*, and twisted by the twist angle θ^*.
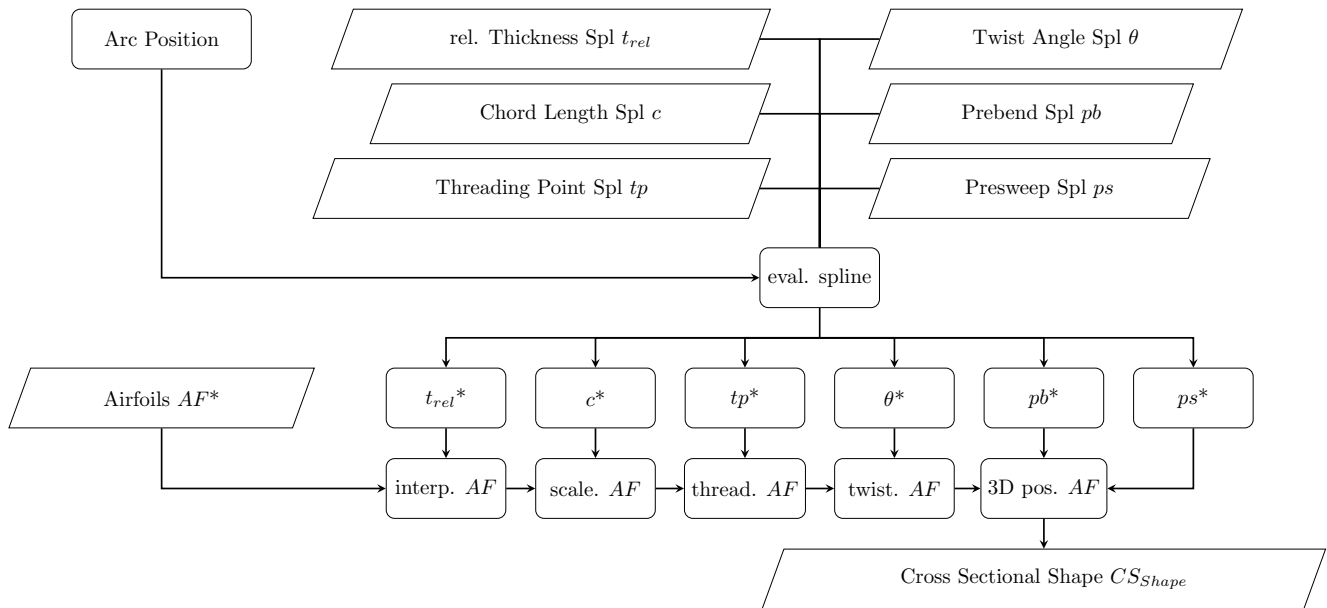
Figure 2. Flowchart of the calculation of the cross-sectional shapes CS_{Shape}.

Until here, all transformations are performed in a 2D chord coordinate system with its final origin in the threading point. The cross-sections are now shifted to the correct 3D position, locating the 2D cross-sectional threading centre on the prebended and preswept global blade axis. By doing so, the 2D chord coordinate system is still parallel to the blade root plane. Hence, the cross-sections are rotated by the slope angles of the prebend and presweep spline functions so that the they are perpendicular to the threading axis. These shifted and rotated cross-sections are the final cross-sectional shapes denoted by CS_{Shape}.

According to figure 1, the next step is the 2D cross-sectional meshing, which is executed using the cross-sectional shapes CS_{Shape} and the parameter sets *Structure*, *Material*, and *Plybook*. This process is presented in figure 3. As before, all data is evaluated for the particular arc positions at the blade segment edges. The division points are generated on the cross-sectional shapes. They serve to subdivide the cross-sections into regions of different material layups. They are also used to define the positions of the shear webs. Then the shapes of the shear web/spar cap and/or trailing edge adhesive joints are computed. The computation of the blade's outer geometry and its structural topology is now finished. After inclusion of the *Material* and *Plybook* information, the FE discretization on 2D cross-section level can be conducted. This yields either a two-dimensional mesh with 4-noded plane elements for the BECAS (DTU Wind Energy) interface or a cross-sectional node map representing a hybrid 2D mesh with 2-noded elements for the composite laminates and 4-noded elements for the adhesives.
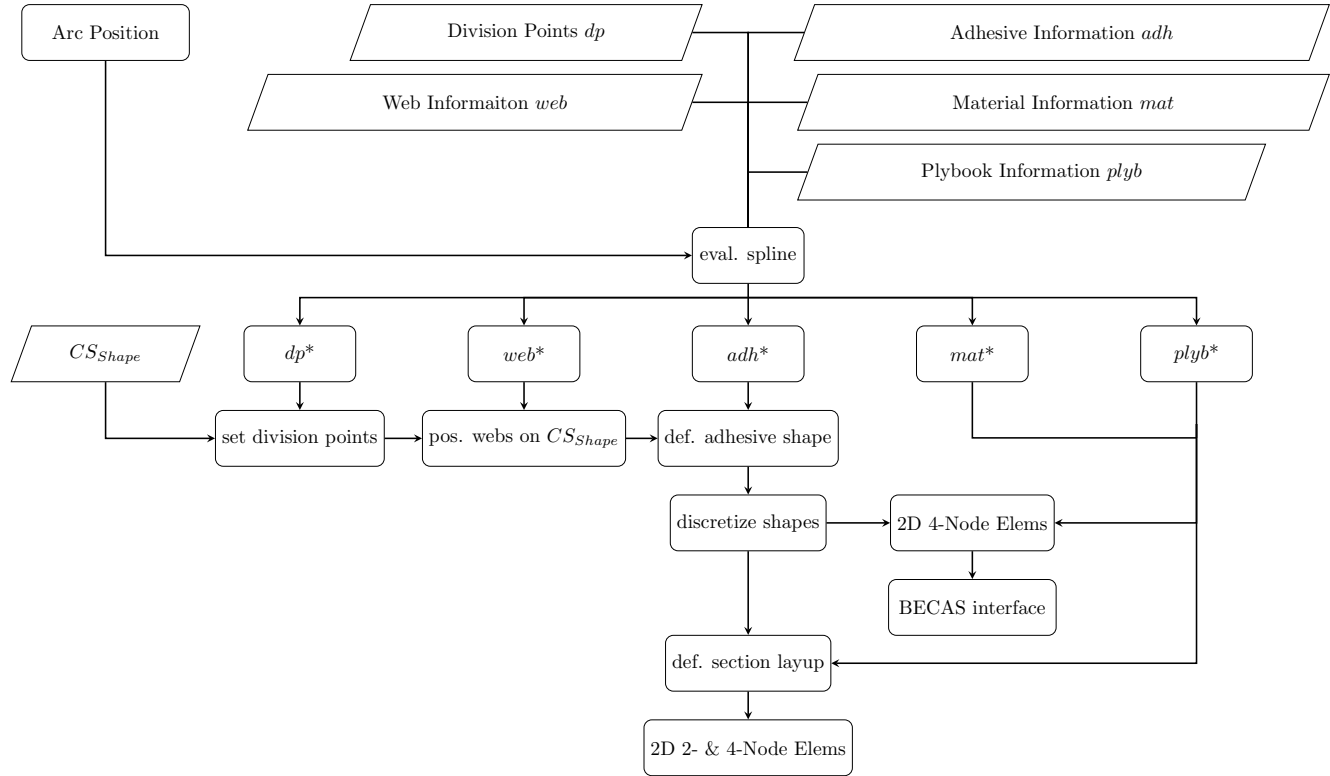
Figure 3. Flowchart of the 2D cross-sectional meshing routine in MoCA.

The last step in the creation of a 3D finite element model is to connect the 2D cross-sectional models, see figure 1. The 2D line elements on the cross-sectional level yield 4-noded shell elements on 3D level after the 3D extension, and the 4-noded plane elements on cross-sectional level become 3D solid elements, respectively.

135 An additional module called *TestRig* is included in MoCA to model the boundary conditions similar to a full scale blade test. Full clamping of the blade root represents the geometrical boundary conditions, i. e. all degrees of freedom are fixed at the blade root. Figure 4 shows the process of the *TestRig* module for the introduction of force-like boundary conditions. In the real blade test, a number of load frames introduces loads that approximate the target bending moment distribution (or torsional moment distribution, respectively). The *TestRig* module approximates the load frames by means of appropriate multiple point

140 constraints MPC and additional masses. For each load frame, the position along the blade (arc position), the load frame width, the centre of gravity (CoG) and the resulting mass are specified as well as the load and sensor points.

In the range where the load frame is located, MoCA searches all elements of the blade shell and defines 2D slave elements that share their nodes. An additional cross-section is created at the desired load frame position according to the procedure depicted in figure 2. In this additional cross-section, the position of the load introduction (load point), the sensor points, and

145 the centre of gravity of the load frame are given in the blade coordinate system. These points are defined as master nodes.

6
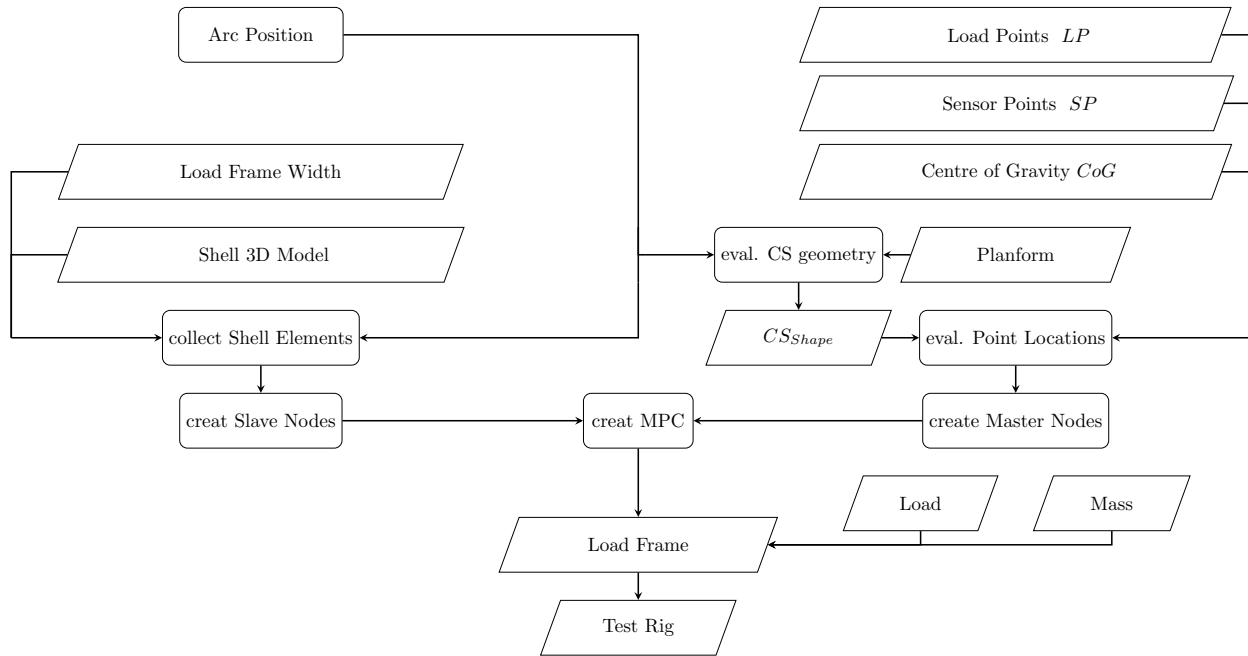
Figure 4. Flowchart of the procedure to model the boundary conditions in the *TestRig* module.

MPCs are included that connect the degrees of freedom of the master nodes and the slave nodes by means of a rigid connection, i. e. there are no relative displacements between the master and the slave nodes. The additional mass of the load frame is applied to the CoG node, while the load is applied to the position where the load is introduced in the real test (load point). In this way, we model solid and quasi-rigid load frames and their effects on the blade response without adding detailed models of the load frames themselves, which is beneficial in the context of computational costs.

The 3D finite element model including the mesh and the boundary conditions is translated to an input file for the finite element solver of choice via an integrated interface.

3 Modelling of the Test Blade

This section briefly describes the blade under consideration, which is the *SmartBlades-DemoBlade*, a 20m long blade with prebend and presweep. It was designed and manufactured in the coordinated research projects *Smart Blades* (Teßmer et al., 2016) and *SmartBlades2* (SmartBlades2, 2016-2020). The blade is abbreviated by *DemoBlade* in the following.

The DemoBlade was designed to investigate bend-twist coupling effects in wind turbine rotor blades. Therefore a presweep of 1 m towards the trailing edge at the tip is intended to introduce a torsional twist into the blade. The offset between the aerodynamic centres of the swept airfoils and the pitch axis introduces a torsional moment and thus a torsional deformation, i. e.

160 a twist in the outer part of the blade. The twist reduces the angle of attack of the respective airfoils and hence the aerodynamic coefficients. In this way the aerodynamic loads can be reduced.

The full blade design of the DemoBlade *as designed* and the manufacturing documentation is available to the authors. In order to allow precise modelling of the DemoBlade *as built* laser scanning of the blade mould was carried out in order to determine the geometry deviations. The derived chord length and absolute thickness distributions for the DemoBlade *as designed*

165 and *as built* can be found in Noever-Castelos et al. (2021). Though the manufacturing deviations in the outer geometry are negligibly small, they will be considered in the modelling process.

After the full scale blade tests, the DemoBlade was cut into segments. The masses and the centres of gravity were determined for all blade segments. The respective procedure will be addressed later in this paper, see sections 4.4 and 5.5. Besides the

170 weighing, the geometry was measured thoroughly in each cut cross-section in order to guarantee the correct positioning of the shear webs in the FE model and to determine deviations from the design due to manufacturing errors. Especially the dimensions of the shear web/spar cap adhesive joints on the pressure side of the blade showed significant deviations to the blade design and had to be adjusted in the FE model. Figure 5 shows the cut at a radial position of 5.2 m. On the suction side we see a nice, thin, and over-laminated shear web/spar cap bonding. However, on the pressure side the shear web/spar cap adhesive joint (which

175 was the blind bond) is much thicker than specified in the design. Moerover, there is a lack of adhesive in large portions of the blade, so that the shear web flanges were not covered entirely by adhesive material. Noever-Castelos et al. (2021) contains the actual dimensions of the pressure side web adhesive.

In the FE model, we apply concentrated and line-distributed additional masses to cover any type of add-ons installed on the blade such as the lightning protection cable or reflectors of an optical sensor system. Noever-Castelos et al. (2021) includes

180 a table wit all additional masses and the respective modelling methods. MoCA furthermore predefines node positions in the blade that correspond to strain gauges installed on the blade. These are documented in Haller and Noever-Castelos (2021). They allow for accurate and easy extraction of strain results at the correct positions.

In advance a mesh convergence study based on strain results at different positions was performed to ensure a qualitatively satisfying mesh density. The resulting base model of the DemoBlade consists of 77,693 elements and 71,781 nodes. A total

185 of 71,016 4-noded shell elements (SHELL181 elements in ANSYS) with offset nodes on the outer blade surface represent the composite components and 6,260 8-noded solid elements (SOLID185 elements in ANSYS) the adhesive joints. All other elements are used to model additional masses in the blade. The only boundary conditions of the base model are the geometric boundary conditions at the blade root (full clamping as described above).

4 Test Description and Virtual Modelling

190 Several test configurations of the full scale blade test were performed to characterize the blade behaviour under different load conditions and to prove that the blade design meets all requirements of the certification guidelines(International Eletrotechnical Comission, 2014). These configurations are than replicated in the virtual test setup and are described in this section.
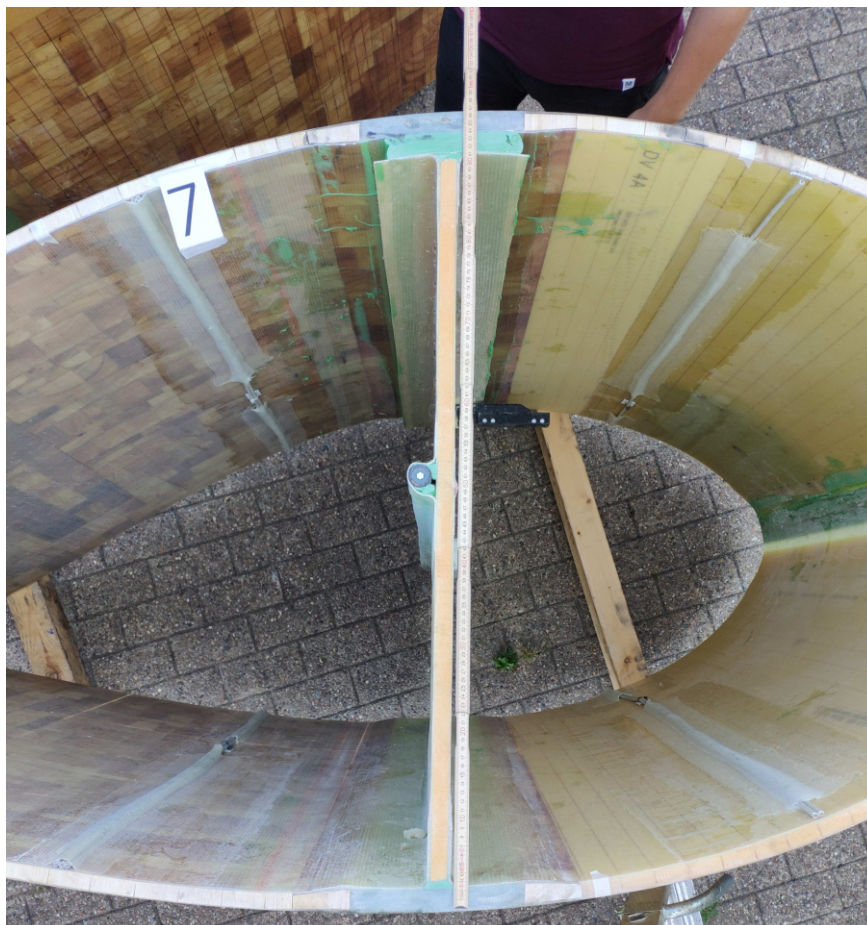
Figure 5. Cut cross-section at a radial position of 5.2 m with a erroneous shear web/spar cap adhesive joint on the pressure side of the blade.

4.1 Mass and Centre of Gravity

The first structural characterization considers the blade's mass and centre of gravity (CoG). An indoor crane equipped with load cells at every hook lifted two points on each root and tip transport structure as shown in Figure 6. As the blade remained still and horizontally suspended the measurements and radial position of each suspension point was recorded. After weighing the transport structures, loading chains and shackles individually, the weight was subtracted from the total recorded load at the measurement devices to obtain the total blade mass. Additionally, the weight of the blade bolts was subtracted from the total mass.

The CoG is obtained by calculating the moment equilibrium with the measured loads with respect to a pivot point, in this case the blade root centre. This procedure was performed for the z-direction (along the span) and y-direction (along the chord).

The mass and CoG of the FE model is calculated during every analysis by default and can be extracted directly from the ANSYS log-file.

9

Figure 6. Setup for mass and centre of gravity measurements.

4.2 Modal Analysis

205   The experimental modal characterization was carried out by the German Aerospace Center (DLR) for different boundary conditions. The methodology is described briefly in the following. For details please refer to Gundlach and Govers (2019).

Free-free boundary conditions were applied after the blade manufacturing by means of elastic suspensions connected to lifting straps. The blade was excited using an impact hammer with soft tip at a total of 8 excitation points. Sensors distributed along the blade recorded the deformations, and the mode frequencies and shapes were extracted from the measurements.

210   The blade was then transported to Fraunhofer IWES and mounted on the test rig. The aim was a second modal characterization with the boundary conditions of the full scale blade test. Electrodynamic long stroke shakers were employed for the excitation of the blade, and sensor outputs were evaluated for the calculation of the mode frequencies and shapes.

During the FE modal analysis, the boundary conditions are adapted to the different characterization tests. In the free-free configuration, no boundary conditions are applied at all, partially resulting in zero eigenvalues related to rigid body motions.

215   These are not considered in the validation process. For the test rig configuration, the blade root is fully clamped, i. e. all 6 degrees of freedom of the shell elements are fixed, for the sake of simplicity. Note that we neglect flexibilities of the bolts and the test rig in this way, which we have to keep in mind when evaluating the simulation results.

4.3 Static Bending and Torsion Test Configuration

The SmartBlades2 DemoBlade was loaded with extreme loads in 4 directions before and after the fatigue test. These four load
220   cases correspond to maximum and minimum edge-wise loading (MXMAX and MXMIN) as well as maximum and minimum
flap-wise loading (MYMAX and MYMIN). Furthermore, three static torsion tests were conducted before the fatigue tests,
in which a torsion moment was applied only at one load frame at a time. The tests are referred to as MZLF2, MZLF3 and
MZLF4, where LFX indicates the particular load frame, in which the torsion moment was introduced. The static tests provide
the necessary information on the structural blade behaviour required to validate the virtual model and test setup.

225   The tests were performed in the facilities of Fraunhofer IWES, where the blade was mounted almost horizontally on a
test rig. The experimental quasi-static loading of the blade is accomplished with a series of horizontally mounted hydraulic
cylinders. These are connected to the load cells via cables which are attached to the load frames mounted on the rotor blade.
Each cable runs through pulleys that are mounted on the floor and redirect the forces from a horizontal to a vertical orientation.
By attaching the load cells to the load frames (load point), the actual load applied to the rotor blade is measured and friction as
well as weight of the loading cables do not affect the measurements. The general test setup is shown in Figure 7.

Figure 7. Photo of a static blade test configuration in flapwise direction.

230

In the following, some general information is given that is valid for all test setups. The test block angle (cone angle) is 7.5° upwards. The coordinate system referred to in this paper has its origin in the centre of the blade root. The y-axis is vertical, the z-axis points horizontally from the origin towards the blade tip (parallel to the floor, not to the pitch axis), and the x-axis follows from the right-hand rule (pointing left watching towards the tip). After turning the blade to the correct position and waiting for a static state, the signals of the load cells and the strain gauges are reset to zero. In the virtual test this is achieved by activating gravity, extracting the deformed nodal coordinates and taking these as the undeformed and stress-free state for the load tests. Gravity is thus not applied in the further analysis and the nodal displacements are virtually reset to zero so that it is easier to postprocess the results. Preliminary verifications showed that the corresponding error is less than 0.5%.

In the tests, four steel load frames with wooden inlays that follow the blade shape at the respective span-wise positions are used to introduce the loads, see Haller and Noever-Castelos (2021). In the following, we refer to the load frames (LF) as LF1 (@ $r = 6.7$m), LF2 (@ $r = 9.7$m), LF3 (@ $r = 14.0$m), and LF4 (@ $r = 17.7$m), where r denotes the span-wise position along the blade. Depending on the test setup, not all load frames are installed. Please refer to Noever-Castelos et al. (2021) to find an overview of all test setups. Each load frame is equipped with two eye-bolts to attach the load cables. These bolts are roughly positioned at the shear centre position in the blade's cross-section to avoid unintended torsion loads. Detailed information on the load frames, such as mass, centre of gravity, and the corresponding shear centre position in the blade's cross-section are given in Haller and Noever-Castelos (2021) .

The test setup is equipped with two different kinds of displacement measurements, an optical displacement measurement system and draw-wire-sensors (DWS). For the model validation in this paper, the DWS signals are considered. Using LINK11-Elements in ANSYS provides a simple and exact model of the draw-wires by defining the attachment points only. The deformation measured by the DWS is then modeled by the element-length variations of the link elements.

All necessary sensor positions (SP) and load introduction points (LP) on the load frames for the different test setups can be found in Haller and Noever-Castelos (2021). At each load frame position, either with or without installed load frame, two DWS are attached. One is connected to a point most to the front bottom corner, i. e. negative y-direction and one at the rear bottom corner, i. e. positive y-direction, of the load frames or blade shells in case no load frame is installed. These two DWS will be referred to as front and rear DWS in the following. At the blade tip, one DWS is attached referred to as Tip DWS. Note that during several load cases, one or the other load frame is not applied due to the setup design, thus the respective DWS have to be attached directly to the blade shell.

The angle between the loading cable and the blade axis can be adjusted in the experiment by changing the pulley block location within a discrete set of fixing points on the floor. Prior to the test setup, the optimal position for each pulley was determined based on the predicted blade deformation and the desired loading cable angle. The applied loads should be aligned to the load frame planes in the deformed configuration. The DWS floor attachment and pulley block positions are specified for each test setup individually.

Additional to the DWS and the optical measurement system, several cross-sections along the blade are equipped with strain gauges, see Haller and Noever-Castelos (2021). The cross-sections at $r = 5$ m and $r = 8$ m are instrumented with strain gauge rosettes (bi-axial strain gauges) with 0°/90° and ±45° orientations. The angles 0° and 90° denote the span-wise and the cross-

section-wise direction, wheres ±45° is defined accordingly. The 0°/90° rosettes are positioned every approx. 250-300 mm along the shell circumference. The ±45° rosettes are located at each web position as well as the leading and trailing edges. Details on strain gauge positions can be found in Haller and Noever-Castelos (2021).

All load cases have the same basic experimental procedure. They were designed to ensure that the actual test matches the specification requirements as closely as possible. Prior to each load case, the rotor blade is rotated to the desired position and mounted to the test stand (with the aforementioned 7.5° cone angle). The load cable pulley blocks are fixed to the appropriate fixation points on the floor. The load cells are installed between the load frames and the loading cables and are then connected to the data acquisition system. Each of the DWS is attached to the blade. The DWS base is positioned so that the wires run perpendicular to the floor. Finally, the loading cables are connected to the hydraulic cylinders.

The tests are then executed in the following order:

1. Functionality check of load cells and displacement sensors.
2. Compensation of load cell and strain gauge measurements (reset to zero).
3. Start data acquisition.
4. Ramp up loads until 100% of the target load, pausing at 40%, 60% and 80% partial loads for 10s each.
5. Ramp down loads, pausing at same load fractions as at ramp up.
6. Stop data acquisition and save measurement data to log file.

The process is similar in the simulation. Starting from the base model, which does not have a cone angle and the blade is positioned with the trailing edge pointing upwards, the steps are as follows:

1. Install necessary load frames.
2. Rotate blade around z-axis to desired position.
3. Include cone angle of test rig (incline the blade by 7.5° upwards around x-axis).
4. Apply gravity and extract new nodal coordinates.
5. Replace old nodal coordinates by the extracted new nodal coordinates (equal to resetting sensors to zero).
6. Apply and ramp up loads onto the LINK11 elements acting as loading cables.
7. Extract element length variation of the LINK11 elements acting as DWS for 40%, 60%, 80% and 100% of the target load.

All individual setups for the simulation with modifications to the base model, all necessary load frames, load points, sensor positions, and forces as well as the corresponding ground positions of the pulley blocks and the DWS attachments are summarized in Haller and Noever-Castelos (2021). The ground position coordinates are given in the blade coordinate system of the base model (no cone angle, or rotation) described above at the beginning of this subsection.

In contrast to the bending tests, the torsion tests have a pair of forces pulling vertically upwards and downwards as shown in figure 8. Because the blade is still mounted at a block angle of 7.5° the torsional moment is not parallel to the pitch axis. The load cable oriented upwards was attached to a ceiling crane and to the load frame at approximately the shear centre position. As the ceiling crane location is hard to record, but the load rope is perpendicular to the ground it was assumed that the location

300 is 30m above (y-direction) the corresponding load point. The force facing downwards was applied onto the load frame corner
on the trailing edge side in order to introduce a torsional moment in that load frame location.
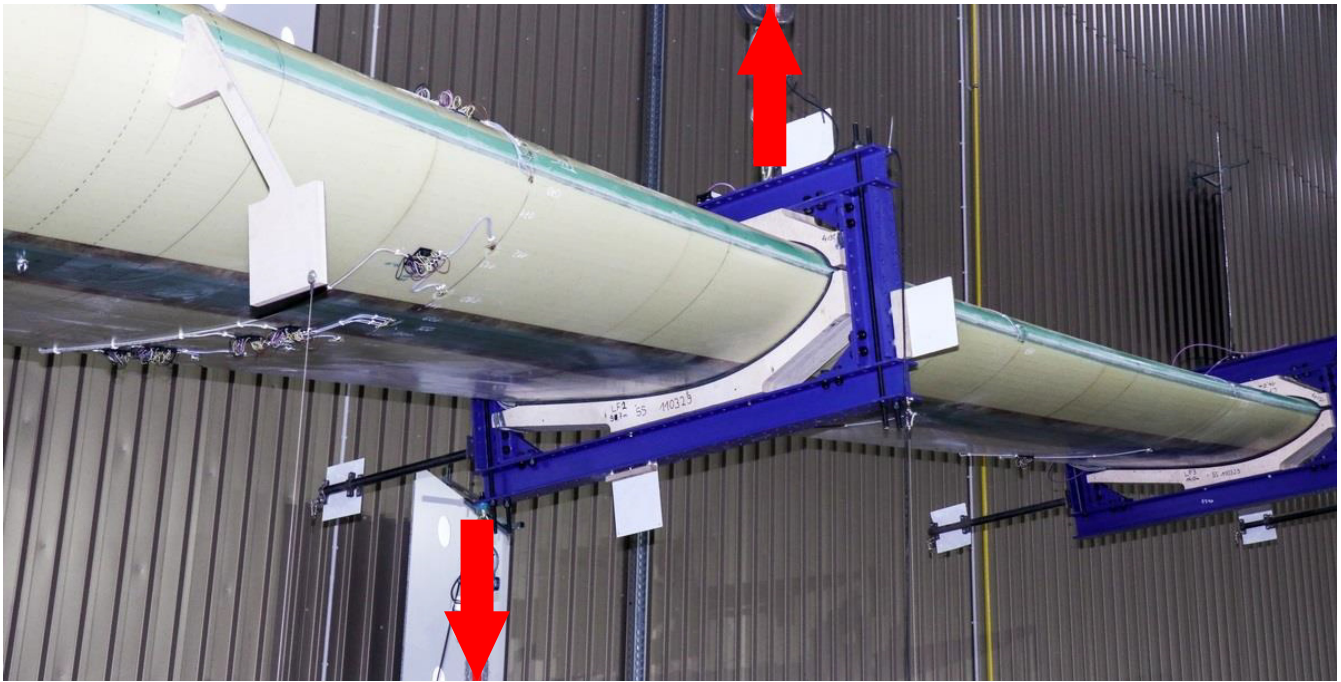
Figure 8. Configuration example of a static torsional loading on the blade with marked up and downwards facing forces.

4.4   Blade Segment Measurement

After finishing the full blade tests, the blade was cut into 17 segments for further characterization. Figure 5 shows a cut surface
of the 7th segment at a span-wise position of $r = 5.2$ m. To determine the 3D centre of gravity (CoG), the segment was suspended
305 at one point with a flexible rope, so that the CoG settled exactly underneath this point (like a pendulum). Hence, the vector in
direction of the suspension rope defines an axis on which the CoG must be located (CoG axis). This procedure was repeated
with different suspension points at least 2 times. The CoG was then found in the intersection point of the different CoG axes.
The measurement setup can be seen in Figure 9 as well as a digital representation of the intersection of different CoG axes.
        To measure the vectors and analyse the data an optical measurement system (photogrammetry) was used. Every segment
310 was equipped with several coded and uncoded reflecting marks to obtain the shape of the segment, the suspension points and
a plummet that was used to get the CoG axes. All the point clouds were analysed in Autodesk Inventor and Siemens NX. All
segments were aligned in CAD and the CoG was extracted for each segment with regard to the blade coordinate system. In this
way we obtained the distribution of the segment CoGs along the blade.
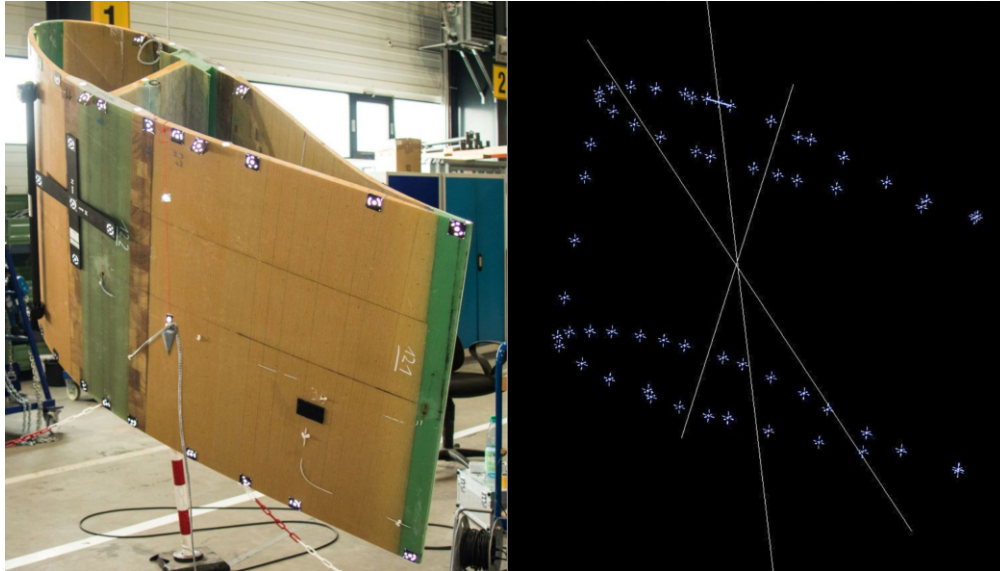
Figure 9. Measurement setup (left) and extracted vectors in CAD with intersection point defining the centre of gravity (right).

Considering the model validation, MoCA is able to generate the respective segments at their correct positions in the blade,
315 so the segment masses and CoGs are a natural output of ANSYS.

5 Comparison of Experimental and Simulation Results

In this section, we compare the experimental results with the simulations. The observation scale will continuously decrease from a global to a more local scale. We start with the global blade characteristics such as eigenfrequencies, total mass, and total centre of gravity. These give a rough estimate of the modeling correctness. Then the blade deformations by means of bending
320 and twist distributions during the static extreme load tests will be analysed. Finally the strain levels in two cross-sections during the extreme load tests and the masses and centres of gravity of the cut blade segments are compared, which give a more detailed view on a local scale.

5.1 Blade Mass, Centre of Gravity, and Eigenfrequencies

Table 1 lists the total blade mass and the location of the centre of gravity in longitudinal (z) and chord direction (y) as well as
325 the measurement uncertainties and the deviation of the numerical model. We see that the model from MoCA is 115.5 kg lighter than the real blade, which corresponds to 6.44% relative difference related to the measurement. In contrast the measurement uncertainty is 45 kg. The mass difference is likely due to manufacturing deviations and/or additional masses (e.g. sensor wires and installations) that have not been considered in the numerical model. The location of the CoG matches perfectly in the

15

chord direction. There is only little deviation of 230 mm in the span-wise direction, which is almost within the measurement
330 uncertainty range of ± 200 mm.

Table 1. Comparison of the total mass and the centre of gravity (CoG).

	Experiment (in kg)	Uncertainty (in kg)	MoCA (in kg)	Difference (in kg)
Mass	1793	45	1673.5	-115.5

CoG	Experiment (in m)	Uncertainty (in m)	MoCA (in m)	Difference (in m)
y	0.10	0.04	0.10	0.00
z	6.58	0.20	6.35	0.23

The results of the modal analysis, both experimental and numerical, are listed in Table 2. The experimental results are
taken from Gundlach and Govers (2019). The flapwise frequencies are in acceptable agreement with deviations of less than
8%. The largest deviation in flapwise modes is found for the 2nd edgewise mode in the test rig configuration (7.94%, which
corresponds to an absolute deviation of 0.54 Hz). The smallest deviation can be observed for the 1st flapwise mode in the
335 free-free configuration, which is 5.83% or 0.28 Hz, respectively. In edgewise direction, the approximation is even better. The
largest relative deviation is seen for the 1st edgewise mode in the test rig configuration, which is 4.84% (or 0.15 Hz in absolute
numbers). The 2nd edgewise mode is only 0.83% (or 0.09 Hz in absolute numbers) smaller in the simulation compared to
the experiment in the test rig configuration, which is an excellent agreement. The largest absolute deviation is present in the
free-free configuration, where the 1st edgewise mode is 0.36 Hz lower than the measured value. Anyways, the deviation of the
340 edgewise modes is less than 5% in all cases, which is a very good agreement. The 1st torsion mode is quite well approximated
in the free-free configuration, where the simulation is 5.62% lower than the experiment. However, in the test rig configuration
the deviation is -11.76% (more than 2 Hz less compared to the test), which is relatively high. In general, the simulations
agree better with the test results in the free-free configuration than in the test rig configuration. This is likely due to the rigid
representation of the test rig and the connection bolts, as already mentioned in section 4.2. Especially in torsion, the flexibility
345 of the test rig may not be negligible.

5.2 Static Bending Tests

The results of the static bending tests will be illustrated by means of deflection lines. For each test setup, two lines exist, one
for the front and one for the rear DWS. The deflections in the front DWS are plotted in Figures 10 for each pausing load during
ramp-up (40 %, 60 %, 80 % and 100 % of the target load as described in section 4.3). The plots for the rear DWS are added in
350 appendix A. A table is added in each of the figures that show the differences between the simulations and the tests (in absolute

Table 2. Comparison of the modal analyses for the free-free (top) and the test rig (bottom) configuration. Experimental results are taken from (Gundlach and Govers, 2019).

Mode free-free	Experiment (in Hz)	MoCA (in Hz)	Difference (in Hz)	Difference (in %)
1st Flap-wise	4.8	5.08	0.28	5.83%
1st Edge-wise	10.1	9.74	-0.36	-3.56%
1st Torsion	16.9	15.95	-0.95	-5.62%

Mode test rig	Experiment (in Hz)	MoCA (in Hz)	Difference (in Hz)	Difference (in %)
1st Flap-wise	2.2	2.37	0.17	7.73%
2nd Flap-wise	6.8	7.34	0.54	7.94%
1st Edge-wise	3.1	3.25	0.15	4.84%
2nd Edge-wise	10.9	10.81	-0.09	-0.83%
1st Torsion	18.7	16.50	-2.20	-11.76%

and relative numbers). The tip DWS values are the same for the rear and the front DWS, as only one DWS is installed at the blade tip.

Figure 10 (a) shows the result of the front DWS during the MXMAX load case. For this scenario a maximum deflection of 180 mm at the blade tip is reached. The simulation shows excellent agreement for the front DWS sensors, with a maximum absolute difference of -2.3 mm at the tip for 100 % load and a maximum relative difference of -4.0 % at LF1, whereas the deviations in all other positions are well below 2.0 %. The rear DWS results shown in figure A1 (a) in appendix A have slightly higher errors with a maximum of -5.5 % at LF1 for full load.

For load case MXMIN, Figure 10 (b) illustrates the front DWS results. Except for LF1 the results are in very good agreement with a maximum deflection error of -1.6 % at LF2 at full load. However, the results in LF1 return maximum errors of 3.8 % at 40 % load, which decreases to 1.8 % at full load. Similar behaviour is found for the rear DWS (Figure A1 (b)); excluding LF1 the maximum error is 1.7 % in LF3 and the tip during 40 % load.

The results of the front DWS during the maximum flap-wise setup (MYMAX, Figure 10 (c)) are in very good agreement, when excluding the LF1 data. The LF1 results tend to show the highest errors. This might probably be due to the smallest absolute deflection values, as a systematic sensor/measurement inaccuracy will have a higher impact on relative errors. Concerning the other load frames the maximum error is found to be -2.6 % for the LF4 DWS at full load, which corresponds to -22.4 mm deflection error at a maximum deflection of 875 mm in the experiment. All other values range between -0.9 % and -2.4 %. The excluded LF1 results show higher errors of up to 9.0 % for 60 % load. For the rear DWS (Figure A1 (c)) though

Case	Load	Unit	LF1	LF2	LF3	LF4	Tip
Difference absolute	40%	mm	-0.1	0.4	0.5	0.1	0.5
	60%	mm	-0.4	0.0	-0.1	-1.1	-0.7
	80%	mm	-0.7	-0.1	-0.4	-1.5	-1.4
	100%	mm	-0.9	-0.2	-0.5	-1.9	-2.3
Difference relative	40%	%	-1.5	2.5	1.3	0.1	0.7
	60%	%	-2.8	0.2	-0.2	-1.2	-0.7
	80%	%	-3.5	-0.2	-0.5	-1.2	-1.0
	100%	%	-4.0	-0.5	-0.5	-1.3	-1.2

Case	Load	Unit	LF1	LF2	LF3	LF4	Tip
Difference absolute	40%	mm	0.4	0.0	0.2	0.2	1.2
	60%	mm	0.4	-0.4	-0.2	-0.3	0.6
	80%	mm	0.5	-0.3	0.3	0.6	2.0
	100%	mm	0.4	-0.8	-0.2	-0.1	1.5
Difference relative	40%	%	3.8	-0.1	0.5	0.3	1.7
	60%	%	2.7	-1.4	-0.4	-0.3	0.5
	80%	%	2.6	-0.8	0.4	0.5	1.3
	100%	%	1.8	-1.6	-0.2	-0.1	0.8

Case	Load	Unit	LF1	LF2	LF3	LF4	Tip
Difference absolute	40%	mm	-2.2	-1.4	-2.4	-6.9	-4.3
	60%	mm	-3.5	-2.3	-3.7	-11.7	-8.4
	80%	mm	-4.5	-3.2	-5.7	-16.9	-14.5
	100%	mm	-5.6	-4.0	-7.3	-22.4	-19.8
Difference relative	40%	%	-8.8	-2.2	-1.3	-2.0	-0.9
	60%	%	-9.0	-2.3	-1.4	-2.2	-1.2
	80%	%	-8.8	-2.4	-1.6	-2.4	-1.6
	100%	%	-8.7	-2.4	-1.6	-2.6	-1.7

Case	Load	Unit	LF1	LF2	LF3	LF4	Tip
Difference absolute	40%	mm	-0.9	-0.3	2.3	4.4	-1.8
	60%	mm	-1.6	-0.8	3.5	7.1	-1.6
	80%	mm	-2.7	-1.9	2.6	6.0	-5.8
	100%	mm	-3.7	-2.8	2.6	6.3	-8.3
Difference relative	40%	%	-4.6	-0.6	1.6	1.7	-0.5
	60%	%	-5.5	-1.0	1.6	1.8	-0.3
	80%	%	-6.8	-1.8	0.9	1.1	-0.8
	100%	%	-7.3	-2.2	0.7	1.0	-1.0

Figure 10. Bending lines extracted from the front draw wire sensor for the (a) MXMAX; (b) MXMIN; (c) MYMAX; (d) MYMIN experiment and simulation. Results are shown for 40%, 60%, 80% and 100% of the target load. The table on the right shows the differences between the simulation and the test.

excluding LF1 (max. error -17.6 %) the LF2 results show errors above 6.7 % with the highest reaching -8.8 % during full load.
For the other two load frames the errors are low again and are between -0.9 % and -2.4 %. If taking a closer look at the LF2
370 full load deflection d in the test and experiment the front DWS shows $d_{Exp,f} = 165$ mm and $d_{Sim,f} = 161$ mm, whereas the
rear DWS returns $d_{Exp,r} = 175$ mm and $d_{Sim,r} = 160$ mm. That means the overall deflection of the simulation is less than in
the experiment but the difference between rear and front is $\Delta d_{Exp} = d_{Exp,r} - d_{Exp,f} = 10$ mm and $\Delta d_{Sim} = -1$ mm, i. e.
the simulation shows a positive twist while the experiment returns a much higher negative twist. The twist angle Θ can be
calculated by the relationship

$$\Theta = arcsin\left(\frac{\Delta d}{l_{SP}}\right), \tag{1}$$

where l_{SP} is the distance of both front and rear DWS attachment points on the load frame. The twist angles becomes
$\Theta_{Exp,LF2} = -0.268°$ in the experiment and $\Theta_{Sim,LF2} = 0.042°$ in the simulation. Assuming the pivot point is at the shear
centre (SC), a correction could be calculated to see if the bad results of the rear DWS at LF2 is due to the wrong twist. All
necessary geometric data can be found in Haller and Noever-Castelos (2021). Following Equation (1) and using the distance
380 of the front or rear DWS attachment to the shear centre, the front absolute difference is increased to -7.87 mm which results
in an error of -4.8 % and the rear deflection is reduced to -7.7 mm, respective -4.4 % during 100 % loading. By this correction
due to a wrong predicted twist angle the rear DWS approximation improves by 4 %, while the accuracy of the front sensor
decreases by only 2.4 %. This correction is introduced to evaluate the accuracy for the bending prediction and only holds for
the LF2 position, as the other positions have different twist angle deviations. Additionally the major influence on the flap-wise
385 loading has to be noted as the DWS attachment distances to the shear centre are much higher than for the edge-wise loading,
i.e. the influence from twist angle deviations is amplified significantly.

Figure 10 (d) shows the front DWS results comparison during the minimum flap-wise loading scenario (MYMIN). All load
frames are installed so can be evaluated and the results show a very good agreement with errors below 2.2 % for all DWS
except LF1. At this first load frame again the results have significantly higher errors of up to -7.3 % at full load. Figure A1 (d)
390 contains the rear DWS result of the MYMIN load case and lists throughout higher deviations of up to -13 % for the LF1 sensor.
Here again, by analysing the twist behaviour of the blade all load frames show significant twist differences and after estimating
a correction, e.g. the accuracy of the LF1 front sensor would decrease to a deviation of -11 %, while that of the rear sensor
increases to -10.4 %. This is the worst approximation of the simulation for the static extreme load bending setups. Anyways,
the other load frames are in very good agreement.

395 ## 5.3 Static Torsion Tests

Full scale blade tests in pure torsion are usually not included in certification processes according to (International Eletrotechni-
cal Comission, 2014) and are thus rarely available. As described in section 4.3 the blade is twisted during three different setups
successively at the load frames LF2, LF3 and LF4. The results of the tests and the simulations are plotted in Figure 11. The
structural behaviour behind the actual loaded frame position to the tip will not be addressed in this paper and is highlighted as
400 grey-coloured areas, as the areas loaded in torsion are located between the root and the respective load frame. Though the raw

results similar to the static bending experiments are the DWS length variation, for these torsional experiments the more relevant twist angles are calculated and plotted according to Equation 1. Figure 11 (a) shows the first torsional test loaded at LF2. The absolute angle deviation from experiment to simulation are in between -0.06° and -0.15° but yields high relative deviation up to 30 % due to the small twist angles of -0.55° at LF1 and -1.72° at LF2 during 100 % load.
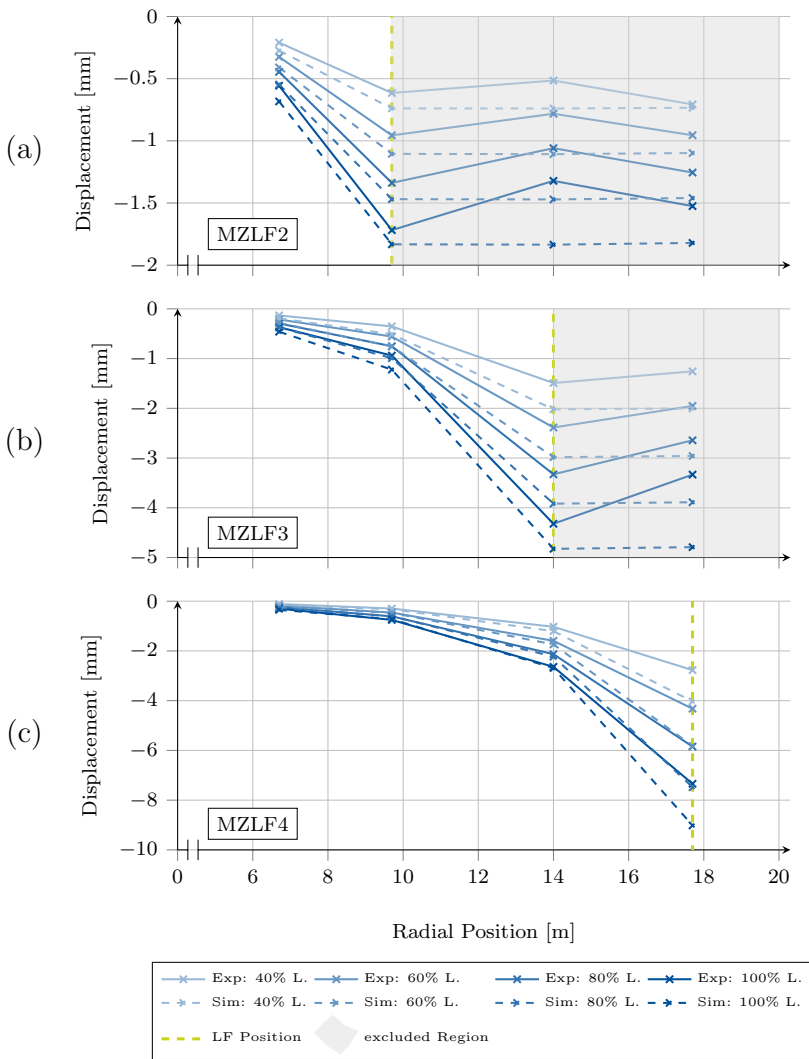
Case	Load	Unit	LF1	LF2	LF3	LF4
Difference absolute	40%	deg	-0.06	-0.12	-0.23	-0.03
	60%	deg	-0.08	-0.15	-0.32	-0.14
	80%	deg	-0.10	-0.13	-0.41	-0.21
	100%	deg	-0.13	-0.11	-0.51	-0.30
Difference relative	40%	%	30.5	20.2	43.8	3.9
	60%	%	26.1	15.6	41.4	15.0
	80%	%	22.9	9.8	39.0	16.4
	100%	%	22.7	6.6	38.7	19.4

Case	Load	Unit	LF1	LF2	LF3	LF4
Difference absolut	40%	deg	-0.06	-0.16	-0.53	-0.75
	60%	deg	-0.07	-0.20	-0.60	-1.01
	80%	deg	-0.08	-0.24	-0.59	-1.25
	100%	deg	-0.09	-0.28	-0.50	-1.46
Difference relative	40%	%	44.0	44.8	35.4	59.3
	60%	%	32.9	35.6	25.0	51.5
	80%	%	27.0	32.0	17.7	47.1
	100%	%	24.9	30.0	11.7	43.7

Case	Load	Unit	LF1	LF2	LF3	LF4
Difference absolut	40%	deg	-0.04	-0.03	-0.18	-1.26
	60%	deg	-0.04	-0.01	-0.14	-1.50
	80%	deg	-0.05	0.01	-0.10	-1.63
	100%	deg	-0.05	0.03	-0.05	-1.68
Difference relative	40%	%	36.1	9.4	17.0	45.5
	60%	%	24.1	2.0	9.1	34.7
	80%	%	19.4	-1.5	4.7	27.9
	100%	%	15.8	-3.7	1.8	22.8

Figure 11. Twist angles calculated from the draw wire sensors results for the (a) LF2; (b) LF3; (c) LF4 torsional loading experiment and simulation. Results are shown for 40%, 60%, 80% and 100% of the target load. The table on the right shows the differences between the simulation and the test.

405   Moving the load application to LF3 (Figure 11 (b)) does not change the situation. At the load application position the absolute error is high with up to -0.6° at a maximum twisting of -4.3°. All errors exceed -10 % dramatically. However, the

experiment with torsional loading on LF4, see Figure 11 (c), shows reasonably good results for the twist angle at LF2 and LF3 with angle deviations of 3.7 % and 1.8 %, respectively. The results at LF4, where the load is applied and which shows the highest twist angle keeps high deviations of about 20 % for full load. Such high errors during torsional loading may base on the
410 shell element with a node offset to the exterior surface used for this model. Pardo and Branner (2005) and especially Laird et al. (2005) already stressed the high inaccuracy of shell elements with node offsets to predict the structural behaviour of hollow structures subjected to torsional loading. However, the twisting is generally overestimated throughout the three torsional tests, which is inline with the aforementioned references.

5.4 Local Strain Comparison

415 As stated in section 4.3 the highly instrumented cross-sections at $r = 5$ m and $r = 8$ m offer a more detailed view on the local strain levels in the rotor blade. The strain results are used to compare the simulations with the tests and to verify that local effects are correctly reproduced. We have selected a few representative load cases in this section. The remaining load cases can be found in appendix B.

In Figure 12 (a) the strain in 0° (span-wise direction, in blue) and 90° (cross-wise, in yellow) directions for the MXMIN
420 simulation (solid lines) and experiment (circles) are plotted over the normalized airfoil circumference (denoted by S) for the 5 m cross-section, starting at the suction side trailing edge ($S = 0$), moving along the suction side to the leading edge ($S \approx 0.5$), and then along the pressure side to the pressure side trailing edge ($S = 1$). This cross-section shows some general characteristics in all load cases, which are:

- In the simulation at $S = 0$, there is a strain peak in the 90° direction, because the sandwich core material vanishes towards
425 the trailing edge.
- In the simulation at $S = 0 - 0.25$, there is an excessive or wrong curvature in the 90° strain curve, for which we do not have a feasible explanation.
- In the simulation at $S = 0.25 - 0.35$, there is a stepped dip or raise of the 90° strain, because the sandwich core material is substituted by core and UD layers and then completely by the UD spar cap and vice versa.
430 - In the simulation at $S = 0.5$, there is a strain peak in the 90° direction, because the sandwich core material vanishes around the leading edge.
- In the experiment at $S = 0.5 - 0.65$, there is a strain dip in the 0° direction, for which we do not have a feasible explanation. The structure should be symmetric next to the leading edge.
- In the simulation at $S = 1$, there is a strain peak in the 90° direction, because the sandwich core material vanishes towards
435 the trailing edge.

Apart from the unclear dip around the suction side leading edge panel ($S = 0.5 - 0.65$), the longitudinal strain (in 0° direction) differs along the circumference only about $\pm 150\ \mu\text{m/m}$. This is about 15 % related to the maximum $\pm 1000\ \mu\text{m/m}$ at the leading or trailing edge. However, the cross-wise strains (in 90° direction) reach deviations of up to $\pm 200\ \mu\text{m/m}$, which corresponds to about 50 % related to its maximum. The MXMAX results (Figure C1 (a)) are very similar concerning maximum
440 values and strain errors.

21
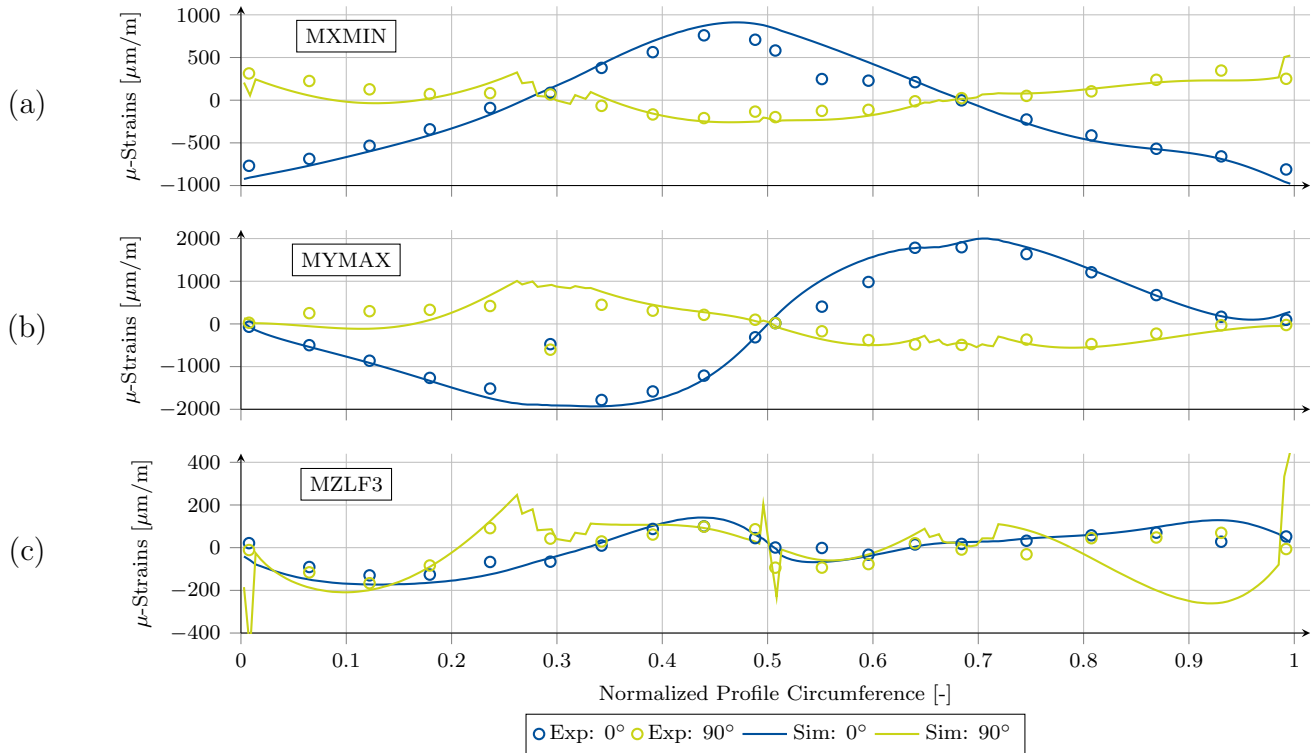
Figure 12. Span-wise and cross-wise strains of the simulation and the test, plotted against the normalized profile circumference of the cross-section at $r = 5$ m for the (a) MXMIN; (b) MYMAX; (c) MZLF3 load case.

Figure 12 (b) shows the MYMAX load case. Unlike the edge-wise case a wrong calibration or malfunction of the strain gauge at $S = 0.3$ was recorded in the experiment. The flap-wise bending of the blade in general is more excessive compared to the edge-wise bending and provokes the highest longitudinal strains in the spar cap positions reaching maximum values of up to $\pm 2000 \ \mu$m/m in the outer shell layer. Consequently the cross-wise strain also increases with maxima of $\pm 500 \ \mu$m/m,

445 both approximately twice as much as in the edge-wise load case. All other aforementioned issues are also present here, some more and some less pronounced. The same conclusion also holds for the MYMIN case in figure C1 (b), though the maximum values are slightly lower, due to smaller load sets.

Taking a look at the torsion tests, in particular for the MZLF3 load case plotted in Figure 12 (c), the longitudinal strain shows a relatively good agreement with the test, except for $S = 0.5 - 0.65$ and at the pressure side trailing edge panel ($S = 0.85 - 1$).

450 The cross-wise strain shows partially good agreement with the experiments, except for the aforementioned characteristics which are more dominant than in the bending tests. E. g. the peaks at the trailing edge is more pronounced. As for the longitudinal strain, the cross-wise strain shows a disagreement between simulation and experimental results, which is even stronger due to a shifted curvature in the plot. These can also be seen during the remaining two torsion tests. The MZLF4 load case in

Figure C1 (d) is very similar to the MZLF3 load case, whereas the MZLF2 load case (Figure C1 (c)) shows all of the stated

455   characteristics in a more pronounced manner as the load introduction is shifted closer to the evaluated section at $r = 5$ m.

The next highly equipped cross-section is at $r = 8$ m. While the previous cross-section was located at maximum chord, this one is already in a region where geometric curvatures are smoother. For direct comparison the same three load cases were selected for this cross-section. As depicted in Figure 13 (a) the longitudinal as well as the cross-wise strains during the MXMIN test follow very well the experimental results, both qualitatively and quantitatively. Strain levels are similar to the cross-section

460   at $r = 5$ m, but the strain errors of the simulation compared to the experiments are much lower (between $\pm 75 \ \mu m/m$). Same holds for the MXMAX loading, see Figure D1 (a), where the strain error is even between $\pm 50 \ \mu m/m$ most of the time. Though these are not very pronounced, the peaks at the trailing and leading edges as well as the stepped dips or raises can be identified as consistent characteristics throughout all test.
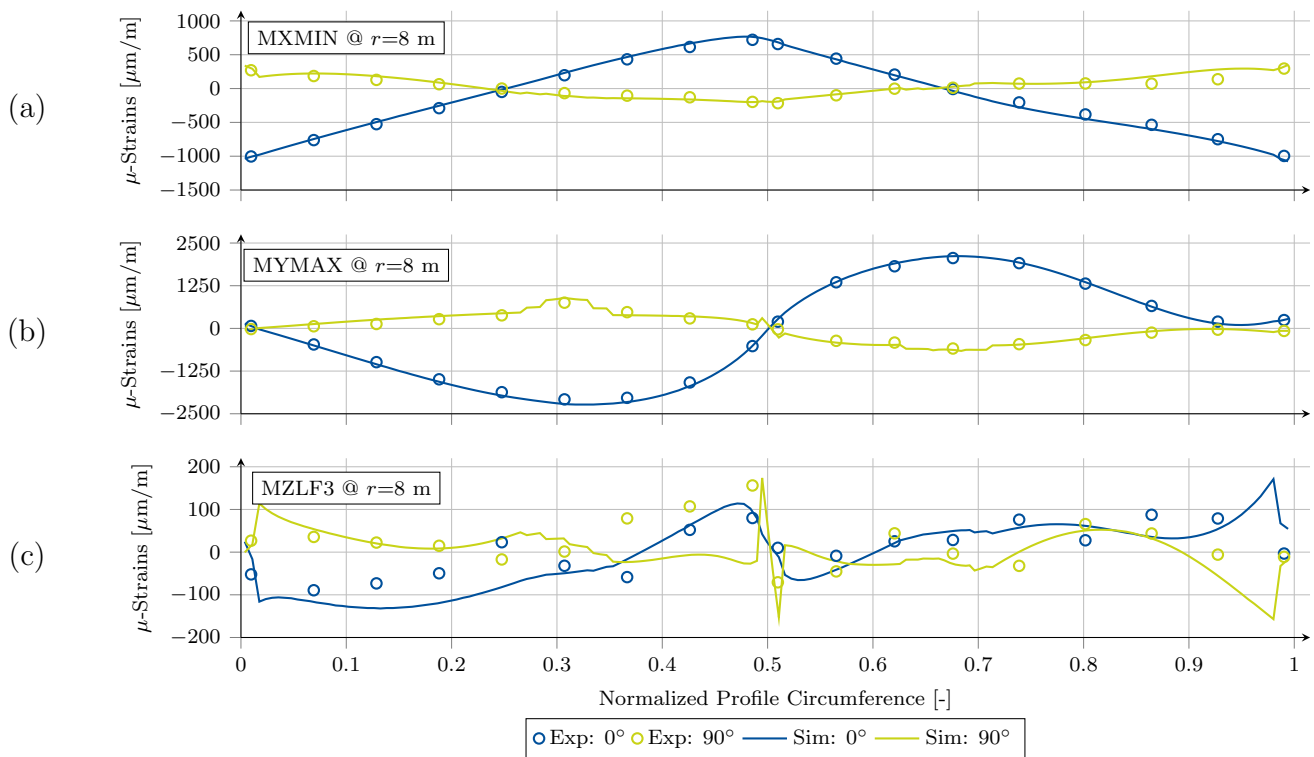
Figure 13. Span-wise and cross-wise strains of the simulation and the test, plotted against the normalized profile circumference of the cross-section at $r = 8$ m for the (a) MXMIN; (b) MYMAX; (c) MZLF3 load case.

Comparing the results of the MYMAX test depicted in Figure 13 (b), the good agreement between the simulation and the

465   test are evident. Even the stepped raise at the two spar caps ($S = 0.3$ and $S = 0.67$) exist in the experimental results. The strain error range is approximately between $\pm 100 \ \mu m/m$, which is less than for the other cross-section, while having slightly higher strain levels. This excellent agreement is also found in figure D1 (b) for the MYMIN load case.

However, the results from the torsional tests do not agree. As seen in figure D1 (c) the simulation results of the longitudinal strain during the MZLF3 test may follow some correct trend of the experiments, but has significant variations. The same applies to the cross-wise strains. Though the strain errors are in the same range as the bending test results, compared to the absolute strain levels these have the same magnitude as the error. The remaining torsional test results (Figure D1 (c) and (d)) show similar problems.

5.5 Segment mass and CoG comparison

In this subsection, we compare the experimental mass and CoG measurement of each segment with the respective simulation results. Table 3 contains the segment numbers, the segment locations along the blade defined by the span-wise positions of the left and the right cutting sections r_1 and r_2, respectively, and the differences of the segment masses and the CoG locations (in absolute and relative numbers).

Table 3. Segment mass and centre of gravity (CoG) differences between experiment and simulation. The relative distances of the CoG are given with respect to their corresponding geometrical cross-section parameter, i. e. absolute thickness (X), chord length (Y), and span-wise segment length (Z).

Section No.	r_1 (in m)	r_2 (in m)	Mass (in kg)	Mass (in %)	Centre of Gravity X (in m)	Centre of Gravity Y (in m)	Centre of Gravity Z (in m)	Centre of Gravity X (in %)	Centre of Gravity Y (in %)	Centre of Gravity Z (in %)
1	0.0	0.9	34.6	9.8%	-0.030	0.000	0.003	-2%	0%	0%
2	0.9	2.0	-7.36	-5.1%	-0.003	0.009	0.035	0%	1%	3%
3	2.0	3.0	-10.96	-9.3%	-0.031	-0.004	0.065	-3%	0%	6%
4	3.0	3.5	-4.74	-8.0%	-0.066	0.000	-0.007	-6%	0%	-1%
5	3.5	4.0	-3.419	-6.1%	-0.076	-0.005	0.021	-8%	0%	4%
6	4.0	5.2	-7.39	-5.9%	-0.094	-0.060	0.055	-10%	-3%	5%
7	5.2	6.5	-6.07	-4.9%	-0.102	-0.036	0.054	-13%	-2%	4%
8	6.5	8.5	-9.81	-5.8%	-0.074	-0.008	0.071	-12%	0%	4%
9	8.5	9.5	-3.572	-4.8%	-0.050	0.007	0.040	-10%	0%	4%
10	9.5	10.5	-5.236	-7.3%	-0.049	0.004	0.132	-11%	0%	13%
11	10.5	11.5	-3.685	-5.4%	-0.041	-0.005	0.108	-10%	0%	11%
12	11.5	12.5	-4.087	-6.6%	-0.031	0.003	0.090	-9%	0%	9%
13	12.5	16.0	-18.59	-9.9%	-0.036	0.007	0.091	-13%	1%	3%
14	16.0	16.5	4.007	16.3%	-0.003	-0.048	0.128	-1%	-4%	26%
15	16.5	17.5								
16	17.5	19.0	-4.405	-9.1%	-0.025	0.094	0.195	-15%	11%	13%
17	19.0	20.0	1.104	9.5%	0.010	0.023	0.041	10%	4%	4%

The relative difference of the mass is related to the measured segment mass and the CoG positions are with respect to the corresponding geometrical mid cross-sectional dimensions, i. e. absolute thickness (X), chord length (Y) and radial segment length(Z). It was not possible to measure segment 15. The mass differs from -4.8 % to -9.9 % except for segment 1,14, and 17,

where the mass was overestimated. Unfortunately it was not possible to calculate an overall blade mass as one segment result was missing. Concerning the CoG differences, the coordinate in cross-section thickness direction (X) varied up to -15 % but was most of the time predicted closer to the suction side. The CoG location in chord direction (Y) agreed very well with the measurement, except for segment 16, the variation were below ±4 %. The radial locations match well for most of the segments

485 (≤ 6 %). However, the sections 10, 11, 12, 14, and 16 resulted in higher variations, predicting the CoG position closer to the tip by more than 10 % of the segment length.

6 Conclusions

The aim of this paper was the validation of a parametrization and modelling methodology for wind turbine rotor blades. This methodology was implemented in the in-house 3D finite element model generator MoCA (Model creation and analysis tool),

490 which creates hybrid shell/solid finite element models.

Full-scale blade tests were performed on the SmartBlades DemoBlade as an experimental reference. The blade has a length of 20 m and is designed with pre-bend and pre-sweep. The following magnitudes were determined experimentally: The total mass and the centre of gravity of the full blade, the mass and centre of gravity distributions along the blade by weighing of blade segments, the natural frequencies in a free-free and a clamped cantilever configuration, the deflection curves along the blade

495 for both flap-wise and edge-wise bending as well as torsion, and the strains in the cross-sectional and longitudinal direction close to the maximum chord position. The governing parameters such as geometry, material layup, manufacturing deviations, additional sensor and load frame masses were extracted from the blade and test documentations. These were fed into MoCA. Finite element models for all test setups were created and the simulations were executed in the commercially available finite element code ANSYS. Then, the simulations were compared with the experimental results.

500 The mass and centre of gravity of the full blade compared very well (error of -6%). The masses and centres of gravity of the blade segments, i. e. the mass and centre of gravity distributions along the blade, were also in good agreement (error of 5-10%). Modal analysis concluded for th natural frequencies with free-free boundary conditions also well (error <6%) matching results, those for the clamped cantilever configuration matched reasonably well (error <8% for bending, 11.7% for torsion).

The deflections for bending in edge-wise direction was in excellent agreement (error <4%). While the deflection curve for

505 bending in flap-wise direction showed a comparably large deviation of 13% at the root, which decreased substantially towards the tip (error at the tip <4%). A reason for that was an elastic twist during the test that was not replicated in the simulations. During torsion, the authors identified quite large deviations in the elastic twist distributions along the blade, because shell models cannot properly replicate torsional behaviour, as is also reported in literature.

For both flap-wise and edge-wise bending the strains in span-wise direction were in very good agreement. Strain gauges

510 were distributed along the circumference of the cross-sections at span-wise positions of 5 m and 8 m, respectively, in order to measure the cross-sectional deformations. There, the authors observed good agreement between the simulations and the experiments, especially at a span of 8 m. However, some local effects close to the spar-caps could not be resolved in the

simulations. In the torsion test, the strains showed quite large deviations. Though, the longitudinal strains agreed sufficiently well, at least qualitatively.

515   Generally speaking, the authors observed good agreement between the simulations and the experiments in almost all situations. The parametrization and modelling methodology can thus be rated as validated. However, there were significant deviations in torsion, which need to be investigated further. The authors currently work on evaluating blade modelling by means of solid elements and/or solid shell elements. In this way, the performance in torsion might be improved significantly.

Code and data availability. The code of MoCA is not publicly available, but may be made available on request at conditions that need to be

520   agreed upon. All experimental and simulation data that support the results of this research as well as the baseline finite element model of the blade as an ANSYS mechanical input file are uploaded in Noever-Castelos et al. (2021)

Appendix A: Static bending test results

(a) MXMAX-Rear
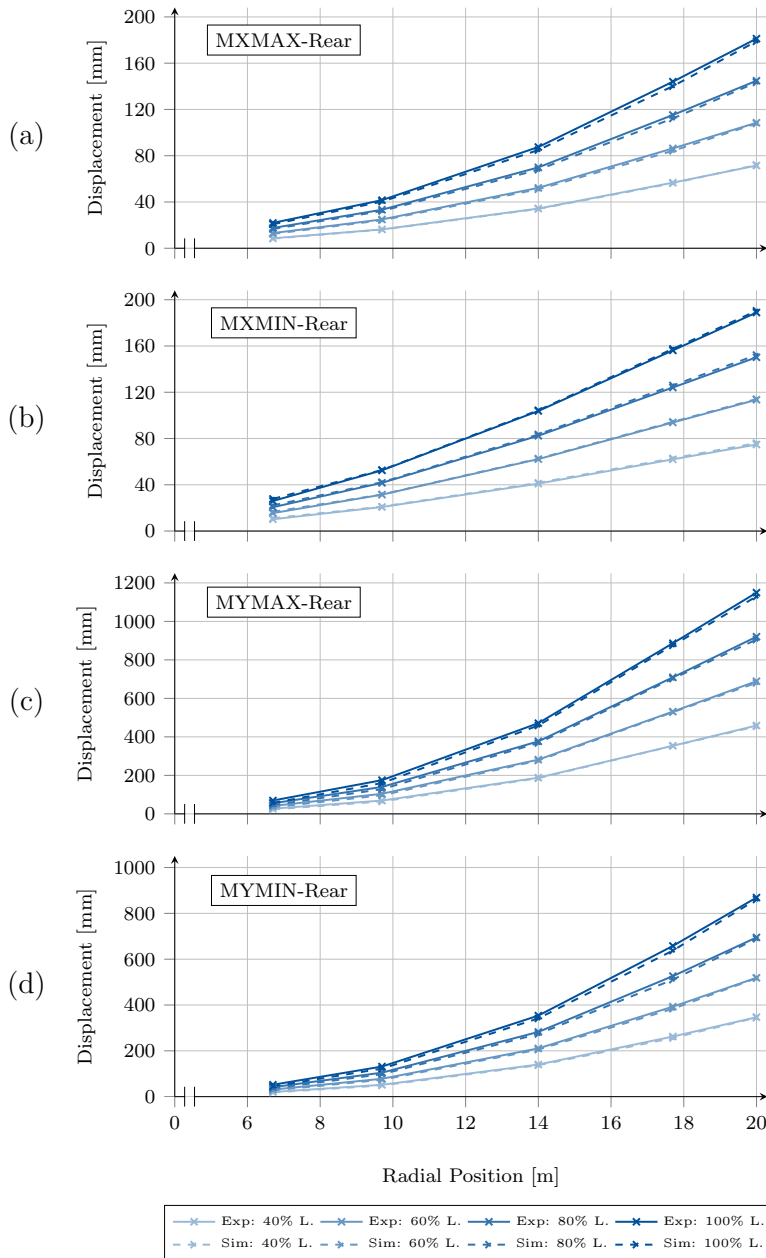
	Case Load	Unit	LF1	LF2	LF3	LF4	Tip
absolute	40%	mm	-0.3	-0.2	-0.3	-0.5	0.5
	60%	mm	-0.7	-0.7	-1.2	-2.1	-0.7
	80%	mm	-0.9	-1.1	-2.0	-3.0	-1.4
	100%	mm	-1.2	-1.3	-2.6	-3.9	-2.3
relative	40%	%	-3.7	-1.0	-0.8	-0.8	0.7
	60%	%	-5.2	-2.8	-2.3	-2.4	-0.7
	80%	%	-5.4	-3.2	-2.8	-2.6	-1.0
	100%	%	-5.5	-3.1	-3.0	-2.7	-1.2

(b) MXMIN-Rear

	Case Load	Unit	LF1	LF2	LF3	LF4	Tip
absolute	40%	mm	0.9	0.3	0.7	0.9	1.2
	60%	mm	1.1	0.1	0.4	0.5	0.6
	80%	mm	1.6	0.5	1.1	1.8	2.0
	100%	mm	1.8	0.3	0.6	1.3	1.5
relative	40%	%	8.5	1.3	1.7	1.4	1.7
	60%	%	7.2	0.4	0.6	0.5	0.5
	80%	%	7.8	1.3	1.3	1.5	1.3
	100%	%	6.9	0.6	0.6	0.8	0.8

(c) MYMAX-Rear

	Case Load	Unit	LF1	LF2	LF3	LF4	Tip
absolute	40%	mm	-4.1	-4.6	-2.7	-0.7	-4.3
	60%	mm	-6.6	-7.9	-4.7	-3.0	-8.4
	80%	mm	-9.3	-11.6	-8.5	-6.7	-14.5
	100%	mm	-12.2	-15.4	-12.2	-10.9	-19.8
relative	40%	%	-15.1	-6.7	-1.4	-0.2	-0.9
	60%	%	-16.0	-7.5	-1.7	-0.6	-1.2
	80%	%	-16.9	-8.3	-2.3	-0.9	-1.6
	100%	%	-17.6	-8.8	-2.6	-1.2	-1.7

(d) MYMIN-Rear

	Case Load	Unit	LF1	LF2	LF3	LF4	Tip
absolute	40%	mm	-2.2	-2.8	-3.2	-6.5	-1.8
	60%	mm	-3.6	-4.4	-5.2	-9.2	-1.6
	80%	mm	-5.1	-6.8	-8.9	-15.4	-5.8
	100%	mm	-6.8	-9.2	-12.3	-20.3	-8.3
relative	40%	%	-10.7	-5.3	-2.2	-2.5	-0.5
	60%	%	-11.8	-5.7	-2.5	-2.4	-0.3
	80%	%	-12.4	-6.5	-3.2	-2.9	-0.8
	100%	%	-13.0	-7.0	-3.5	-3.1	-1.0

Legend: Exp: 40% L. · Exp: 60% L. · Exp: 80% L. · Exp: 100% L. · Sim: 40% L. · Sim: 60% L. · Sim: 80% L. · Sim: 100% L.

Figure A1. Bending lines extracted from the rear draw wire sensor for the (a) MXMAX; (b) MXMIN; (c) MYMAX; (d) MYMIN experiment and simulation. Results are shown for 40%, 60%, 80% and 100% of the target load. The table on the right shows the differences between the simulation and the test.

Appendix B: Local strain comparison
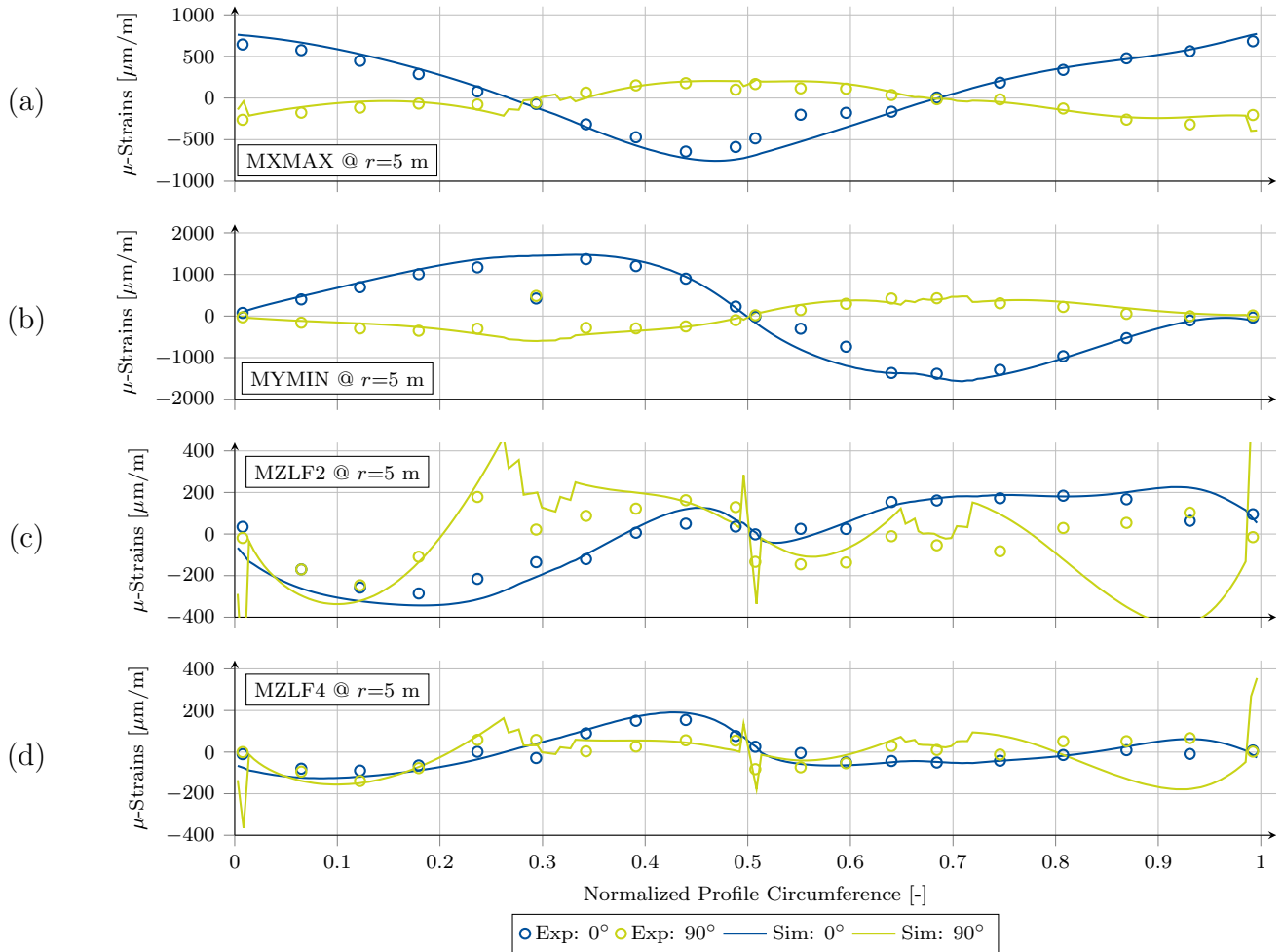
Figure C1. Span-wise and cross-wise strains of the simulation and the test, plotted against the normalized profile circumference of the cross-section at $r = 5$ m for the (a) MXMAX; (b) MYMIN; (c) MZLF2; (d) MZLF4 load case.
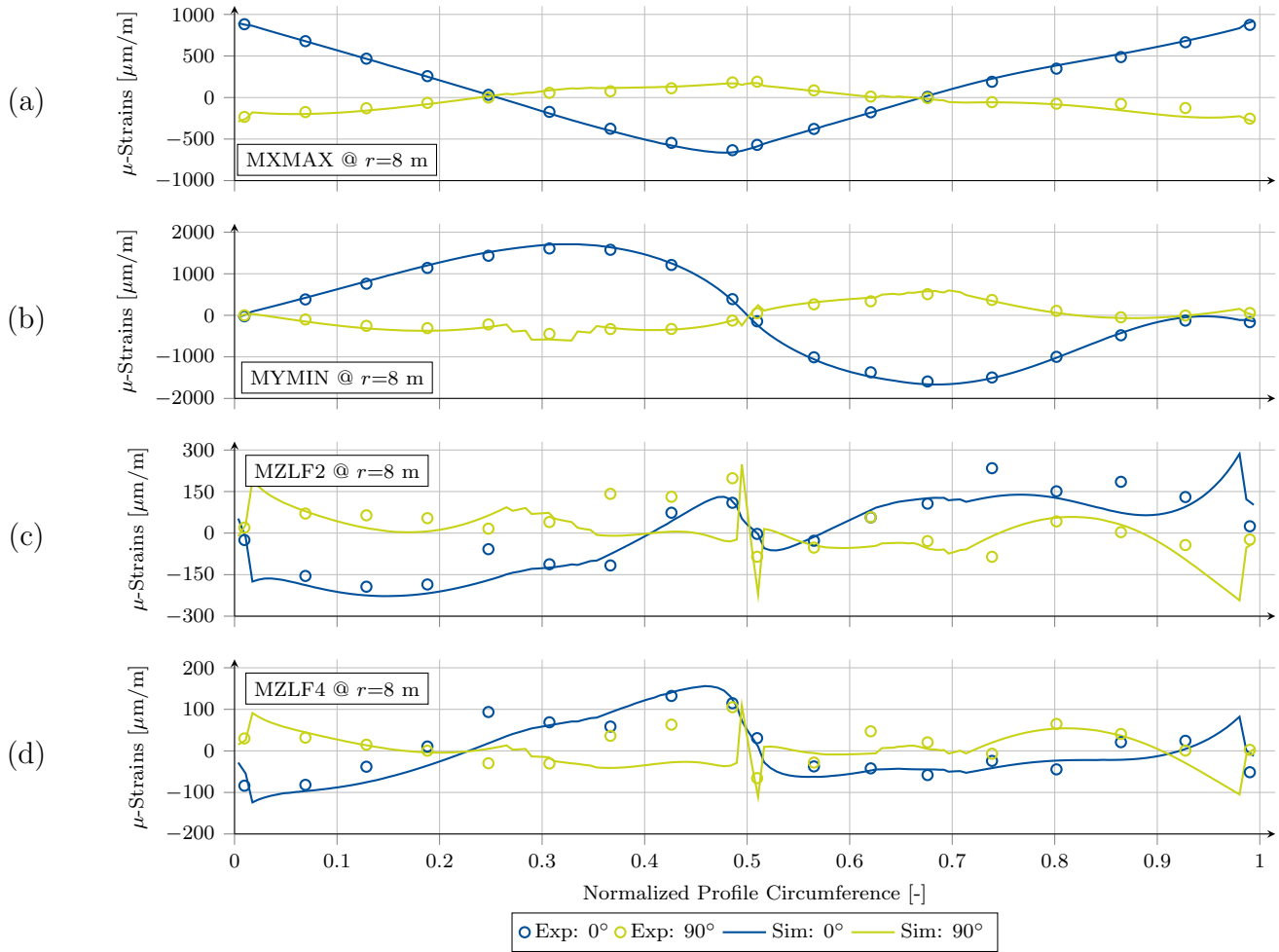
Figure D1. Span-wise and cross-wise strains of the simulation and the test, plotted against the normalized profile circumference of the cross-section at $r = 8$ m for the (a) MXMAX; (b) MYMIN; (c) MZLF2; (d) MZLF4 load case.

Author contributions. Pablo Noever-Castelos implemented the parametrization and modeling methodology in MoCA, conducted the numer-
ical simulations, compared the simulations with the tests, and wrote the paper. Bernd Haller planned, executed, and documented the tests.
Claudio Balzani is the supervisor and guided Pablo Noever-Castelos in the conception of the ideas and participated in the specification of
strain gauge positions as well as in writing, structuring, and reviewing the paper.

Competing interests. The authors declare that they do not have any conflicts of interests.

References

535 ANSYS Inc.: Ansys® Academic Research Mechanical, Release 19.2.

Bottasso, C. L., Campagnolo, F., Croce, A., Dilli, S., Gualdoni, F., and Nielsen, M. B.: Structural optimization of wind turbine rotor blades by multilevel sectional/multibody/3D-FEM analysis, Multibody System Dynamics, 32, 87–116, https://doi.org/10.1007/s11044-013-9394-3, 2014.

C. Bak, F. Zahle, R. Bitsche, T. Kim, A. Yde, L.C. Henriksen, P.B. Andersen, and A.: Design and performance of a 10 MW wind turbine, 540 Wind Energy, 2013.

Chen, H., Yu, W., and Capellaro, M.: A critical assessment of computer tools for calculating composite wind turbine blade properties, Wind Energy, https://doi.org/10.1002/we.372, 2010.

Chen, X., Zhao, W., Zhao, X., and Xu, J.: Failure Test and Finite Element Simulation of a Large Wind Turbine Composite Blade under Static Loading, Energies, 7, 2274–2297, https://doi.org/10.3390/en7042274, 2014.

545 Chen, X., Zhao, X., and Xu, J.: Revisiting the structural collapse of a 52.3 m composite wind turbine blade in a full-scale bending test, Wind Energy, 20, 1111–1127, https://doi.org/10.1002/we.2087, 2017.

D. Marten, J. Wendler, G.Pechlivanoglou, C. N. Nayeri, and C. O. Paschereit: QBlade: An open source tool for design and simulation of horizontal and vertical axis wind turbines, International Journalof Emerging Technology and Advanced Engineering, 2013.

DTU Wind Energy: User's Manual for BECAS – A cross section analysis tool for anisotropic and inhomogeneous beam sections of arbitrary 550 geometry.

Eder, M. A. and Bitsche, R. D.: Fracture analysis of adhesive joints in wind turbine blades, Wind Energy, 18, 1007–1022, https://doi.org/10.1002/we.1744, 2015.

Gundlach, J. and Govers, Y.: Experimental modal analysis of aeroelastic tailored rotor blades in different boundary conditions, Journal of Physics: Conference Series, https://doi.org/10.1088/1742-6596/1356/1/012023, 2019.

555 Ha, K., Bätge, M., Melcher, D., and Czichon, S.: Development and feasibility study of segment blade test methodology, Wind Energy Science, 5, 591–599, https://doi.org/10.5194/wes-5-591-2020, 2020.

Haller, B. and Noever-Castelos, P.: Full scale blade test of a 20 m wind turbine blade within the SmartBlades2 project, https://doi.org/10.5281/zenodo.4605409, 2021.

International Eletrotechnical Comission: IEC 61400-23: Wind turbines - Part 23: Full-scale structural testing of rotor blades, 2014.

560 Jensen, F. M., Falzon, B. G., Ankersen, J., and Stang, H.: Structural testing and numerical simulation of a 34m composite wind turbine blade, Composite Structures, 76, 52–61, https://doi.org/10.1016/j.compstruct.2006.06.008, 2006.

Ji, Y. M. and Han, K. S.: Fracture mechanics approach for failure of adhesive joints in wind turbine blades, Renewable Energy, 65, 23–28, https://doi.org/10.1016/j.renene.2013.07.004, 2014.

Jonathan C. Berg and Brian R. Resor: Numerical Manufacturing And Design Tool (NuMAD v2.0) for WInd Turbine Blades: User's Guide, 565 2012.

Laird, D., Montoya, F., and Malcolm, D.: Finite Element Modeling of Wind Turbine Blades, p. 354, https://doi.org/10.2514/6.2005-195, 2005.

Lekou, D. J., Bacharoudis, K. C., Farinas, A. B., Branner, K., Berring, P., Croce, A., Philippidis, T. P., and de Winkel, G. D.: A Critical Evaluation of Structural Analysis Tools used for the Design of Large Composite Wind Turbine Rotor Blades under Ultimate and Cycle

570   Loading, A Critical Evaluation of Structural Analysis Tools used for the Design of Large Composite Wind Turbine Rotor Blades under Ultimate and Cycle Loading, 2015.

N. P. Duineveld: Structure and Possibilities of the FOCUS Desgin Package, 2008.

Noever-Castelos, P., Haller, B., and Balzani, C.: Supplement to: Validation of a modelling methodology for wind turbine rotor blades by means of a full scale blade test, https://seafile.cloud.uni-hannover.de/d/d0f144c6b65042cbb060/, 2021.

575   Overgaard, L. and Lund, E.: Structural collapse of a wind turbine blade. Part B: Progressive interlaminar failure models, Composites Part A: Applied Science and Manufacturing, 41, 271–283, https://doi.org/10.1016/j.compositesa.2009.10.012, 2010.

Overgaard, L., Lund, E., and Thomsen, O. T.: Structural collapse of a wind turbine blade. Part A: Static test and equivalent single layered models, Composites Part A: Applied Science and Manufacturing, 41, 257–270, https://doi.org/10.1016/j.compositesa.2009.10.011, 2010.

Pardo, D. R. and Branner, K.: Finite Element Analysis of the Cross-Section of Wind Turbine Blades; A Comparison between Shell and

580   2D-Solid Models, Wind Engineering, 29, 25–31, https://doi.org/10.1260/0309524054353700, 2005.

Peeters, M., Santo, G., Degroote, J., and van Paepegem, W.: High-fidelity finite element models of composite wind turbine blades with shell and solid elements, Composite Structures, 200, 521–531, https://doi.org/10.1016/j.compstruct.2018.05.091, 2018.

Reder, M. D., Gonzalez, E., and Melero, J. J.: Wind Turbine Failures - Tackling current Problems in Failure Data Analysis, Journal of Physics: Conference Series, 753, https://doi.org/10.1088/1742-6596/753/7/072027, 2016.

585   Rosemeier, M.: FEPROC Blade Model Verification - 3D Shell and Beam Model, https://doi.org/10.5281/ZENODO.1493936, 2018.

SmartBlades2: Fabrication, Testing, and Further Development of Smart Rotor Blades, coordinated research project (project numbers 0324032A-H), supported by the Federal Ministry for Economic Affairs and Energy of Germany due to a decision of the German Bundestag, 2016-2020.

Teßmer, J., Icpinar, C., Sevinc, A., Daniele, E., Riemschneider, J., Hölling, M., and Balzani, C.: Schlussbericht Smart Blades: Technical

590   Report, 2016.

Yu, W., Volovoi, V. V., Hodges, D. H., and Hong, X.: Validation of the Variational Asymptotic Beam Sectional Analysis, AIAA Journal, 40, 2105–2112, https://doi.org/10.2514/2.1545, 2002.

Zahle, F.: PGL - Parametric Geometry Library, https://gitlab.windenergy.dtu.dk/frza/PGL, 2020.

Zahle, F., Réthoré, P.-E., Graf, P., Dykes, K., and Ning, A.: FUSED-Wind dev, https://github.com/FUSED-Wind, 2020.